Pergamon

Int. J. Heat Mass Transfer. Vol. 39, No. 10, pp. 2095–2113, 1996

0017-9310/96 $15.00 + 0.00

0017-9310(95)00279-0

The effects of liquid–vapor coupling and non-Darcian transport on asymmetrical disk-shaped heat pipes

N. ZHU and K. VAFAI†

Department of Mechanical Engineering, The Ohio State University, Columbus, OH 43210, U.S.A.

(*Received* 11 *April* 1995 *and in final form* 21 *July* 1995)

Abstract—In this work a pseudo-three-dimensional analytical model is developed for the steady incompressible vapor and liquid flow in an asymmetrical disk-shaped heat pipe. The hydrodynamic coupling of the vapor and liquid flow, the gravitational effects and the effects of non-Darcian transport through the porous wick are incorporated in the model, and the variations in upper and lower liquid velocity and pressure distributions are accounted for. The asymmetrical vapor and upper and lower liquid velocity profiles, the vapor and upper and lower liquid pressure distributions and the interface temperature distribution accounting for the vapor–liquid coupling and the non-Darcian effects are obtained. The effects of the vapor-liquid coupling, upper and lower liquid velocity and pressure fields and boundary and inertia in altering the limiting heat pipe heat transfer performance are discussed and assessed. Finally, the analytical results are compared with the available experimental data and are found to be in good agreement. Copyright © 1996 Elsevier Science Ltd.

INTRODUCTION

Asymmetrical heat pipes have received some attention recently in several application areas such as the cooling of electronic equipment, high-performance space applications and other commercial thermal devices. The investigations of asymmetrical heat pipes have focused mainly on the experimental testing of the heat pipe performance. Analysis of flow and heat transfer characteristics of an asymmetrical heat pipe is given by Vafai and Wang [1] and Vafai *et al.* [2]. They developed a pseudo-three-dimensional analytical model for the steady incompressible vapor and liquid flow in flat plate and disk-shaped heat pipes and obtained analytical results for the vapor velocity profile, the vapor and liquid pressure distributions and the liquid–vapor interface temperature distribution, as well as the maximum heat transfer capability of both types of heat pipes. They also performed the parametric study for the optimum performance of both types of heat pipes.

The analyses of cylindrical and annular heat pipes with a symmetrical heat source and sink have been performed extensively by many investigators. These investigations include both analytical and numerical methods, transient and steady conditions as well as one- or two-dimensional modeling. The majority of these investigators focused their work on the dynamics of the vapor flow. The liquid flow was mostly neglected by using one- or two-dimensional heat conduction models for the liquid–wick region. Ransom and Chow [3], Doster and Hall [4], and Tournier and El-Genk [5] incorporated liquid flow in their numerical investigations of cylindrical heat pipes. The coupling of the vapor and liquid momentum equations was done by applying either the Laplace–Young equation [3, 4] or the complete form of the momentum jump condition in the normal direction [5] at the liquid–vapor interface. In their studies, the matching conditions of velocity and shear stress were neglected by assuming a non-slip condition and neglecting the interfacial drag at the liquid–vapor interface. Furthermore, the boundary and inertial effects on the heat pipe operation have not been investigated in the open literature, nor has there been any theoretical analysis of these effects.

For asymmetrical heat pipes the liquid flow is significantly more complicated and the effects of liquid flow are more prominent. Vafai and co-workers [1, 2] have incorporated liquid flow in their analytical investigation of asymmetrical flat plate and disk-shaped heat pipes. However, they assumed the same liquid flow rates in both top and bottom wicks by applying Darcy's law to the liquid flow. They have also neglected the hydrodynamic coupling of the vapor and liquid flow as well as the non-Darcian effects in their analysis.

In the present work the generalized momentum equation in porous media is utilized in a pseudo-three-dimensional analytical model for predicting the performance of a disk-shaped heat pipe heated from the top surface. The coupling of the vapor and liquid flow is established through matching conditions at the vapor–liquid interfaces and the coupled vapor and liquid momentum equations are solved simultaneously. The coupling of the liquid flow within the

† Author to whom correspondence should be addressed.

NOMENCLATURE

A_e	evaporator area [m^2]
f	location of the maximum vapor velocity [m]
g	gravitational acceleration
h	height of vapor space for the heat pipe [m]
h_{fg}	latent heat of working fluid [kJ kg^{-1}]
h_w	thickness of the top and bottom wicks [m]
h_{wv}	thickness of the vertical wicks [m]
K	permeability of the top and bottom wicks [m^2]
K_v	permeability of the vertical wicks [m^2]
p	vapor pressure [Pa]
Q	liquid flow rate in a vertical wick at location r [m^2 s^{-1}]
r, y	radial and vertical coordinates [m]
R	radius of the disk-shaped heat pipe [m]
$\bar{R}$	ideal gas constant, $\bar{R} = 8.31433$ [kJ (kmol·K)$^{-1}$]
Re_h	injection Reynolds number, $\rho_v v_1 h/\mu_v$
T	temperature [K]
u, v, w	radial, vertical, angular velocity components [m s^{-1}]
U	the maximum radial velocity component [m s^{-1}]
$\mathbf{v}$	volume-averaged velocity vector
v_1	vapor injection velocity [m s^{-1}]
v_2	vapor suction velocity [m s^{-1}].

Greek letters

ε	porosity of the top and bottom wick structure
φ	square root of the ratio of the evaporator area to the heat pipe area, $\varphi^2 = A_e/\pi R^2$
Φ	angle of each divergent flow channel of disk-shape heat pipe
γ	the top and bottom porous wick shape parameter, $\sqrt{\varepsilon/K}$
μ	dynamic viscosity [N s m^{-2}]
θ	angular coordinate
ρ	density [kg m^{-3}].

Subscripts

i	vapor–liquid interface
l	liquid phase
v	vapor phase.

Superscripts

b	the bottom wick
t	the top wick
+	dimensionless quantity.

top and bottom wicks is established by the balance of mass and momentum of the liquid flow within the vertical wicks. Analytical results for the asymmetrical vapor and liquid velocity profiles, the vapor and liquid pressure distributions and the interface temperature distribution accounting for the interfacial and non-Darcian effects are obtained. The effect of the hydrodynamic coupling of the vapor and liquid phases and the effects of non-Darcian transport through the porous wick on the vapor and liquid velocity profiles, the vapor and liquid pressure distributions and the interface temperature distribution are investigated at length. The effects of the vapor-liquid coupling and boundary and inertia on the maximum heat transfer capability of the heat pipe are also discussed. In addition, the analytical model is used to simulate the disk-shaped heat pipe tested by North and Avedisian [6] and a good agreement is found between the predicted maximum heat transfer and the measured data.

FORMULATION AND ANALYSIS

The schematic diagram of the disk-shaped heat pipe for the present investigation is shown in Fig. 1. Heat input is over an area $A_e = \pi(\varphi R)^2$ on the top surface of the heat pipe. This results in vaporization and subsequent pressurization of the liquid around the heated region. Condensation of the vapor occurs on the bottom wick and the outer edge of the top wick. The vapor space is divided into several channels by vertical wicks which transport liquid from the bottom wick to the top wick. Any one of the internal channels can be considered as a building block for the disk-shaped heat pipe. Therefore, we will concentrate on the fluid flow considerations within one of these channels (Fig. 1b). Once the fluid flow characteristics within one of the channels are determined, the fluid flow characteristics of the entire heat pipe can be easily established. The results of this analysis are applicable to any number of channels, any specified thickness of the wicks, any specified thickness and any specified overall radius of the disk-shaped heat pipe.

In the present analysis, vapor and liquid flows are assumed to be steady, laminar and incompressible. In addition, the transport properties of the vapor and liquid are assumed to be constant. All wicks are assumed isotropic and saturated with wetting liquid. The liquid and the vapor regions are separated by a

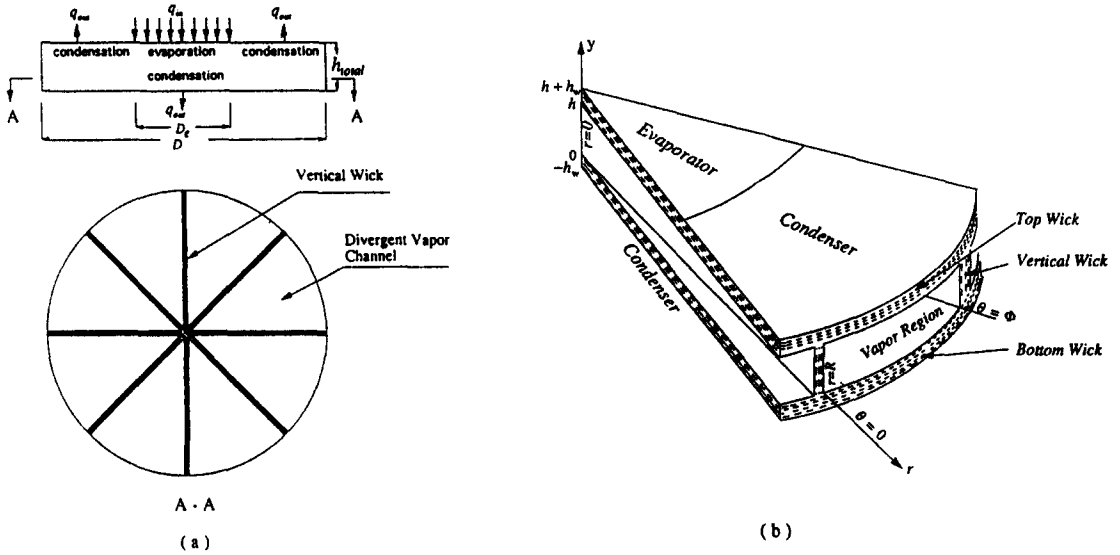

Fig. 1. Schematic of the disk-shaped heat pipe: (a) geometry of the heat pipe, (b) the coordinate system used in the analysis.

distinct boundary (vapor–liquid–wick interface), with no two-phase zone in between. The vapor injection and suction rate are assumed uniform on the top and bottom wicks and negligible on the vertical wicks. Therefore, the vapor velocity component in the θ direction is negligible.

The mathematical model of the vapor and liquid flow within a channel is described by three subregions: the top liquid–wick region, the vapor region and the bottom liquid–wick region (Fig. 1b), each of which has its own set of governing equations. In the vapor region, the continuity and r-momentum equations are

$$\frac{\partial u_v}{\partial r}+\frac{\partial v_v}{\partial y}+\frac{u_v}{r}=0 \tag{1}$$

$$\rho_v\left(u_v\frac{\partial u_v}{\partial r}+v_v\frac{\partial u_v}{\partial y}\right)=-\frac{\partial p_v}{\partial r}+\mu_v\left(\frac{\partial^2 u_v}{\partial r^2}+\frac{1}{r}\frac{\partial u_v}{\partial r}-\frac{u_v}{r^2}+\frac{\partial^2 u_v}{\partial y^2}+\frac{1}{r^2}\frac{\partial^2 u_v}{\partial\theta^2}\right). \tag{2}$$

The conservation equations for the liquid flow within top and bottom wicks are based on the generalized momentum equation [7] which account for the boundary and inertial effects. The convective term in the generalized momentum equation is dropped in accordance with the work of Vafai and Tien [7]. The governing equations for the liquid flow in the bottom wick are

$$\frac{1}{r}\frac{\partial}{\partial r}(ru_l^b)+\frac{\partial v_l^b}{\partial y}+\frac{1}{r}\frac{\partial w_l^b}{\partial\theta}=0 \tag{3}$$

$$\frac{\mu_l}{\varepsilon}\left(\frac{\partial^2 u_l^b}{\partial r^2}+\frac{1}{r}\frac{\partial u_l^b}{\partial r}-\frac{u_l^b}{r^2}+\frac{\partial^2 u_l^b}{\partial y^2}+\frac{1}{r^2}\frac{\partial^2 u_l^b}{\partial\theta^2}\right)-\frac{\mu_l}{K}u_l^b-\frac{\rho_l F\varepsilon}{K^{1/2}}|\mathbf{v}_l^b|u_l^b-\frac{\partial p_l^b}{\partial r}=0 \tag{4}$$

and for the liquid flow in the top wick are

$$\frac{1}{r}\frac{\partial}{\partial r}(ru_l^t)+\frac{\partial v_l^t}{\partial y}+\frac{1}{r}\frac{\partial w_l^t}{\partial\theta}=0 \tag{5}$$

$$\frac{\mu_l}{\varepsilon}\left(\frac{\partial^2 u_l^t}{\partial r^2}+\frac{1}{r}\frac{\partial u_l^t}{\partial r}-\frac{u_l^t}{r^2}+\frac{\partial^2 u_l^t}{\partial y^2}+\frac{1}{r^2}\frac{\partial^2 u_l^t}{\partial\theta^2}\right)-\frac{\mu_l}{K}u_l^t-\frac{\rho_l F\varepsilon}{K^{1/2}}|\mathbf{v}_l^t|u_l^t-\frac{\partial p_l^t}{\partial r}=0. \tag{6}$$

The vapor and liquid phases are coupled at the liquid–vapor interfaces, $y=0$ and $y=h$. The continuity of mass fluxes in the y-direction at these interfaces yields

$$\rho_v v_v(r,y=0,\theta)=\rho_l v_l^b(r,y=0,\theta)=-\rho_v v_2 \tag{7}$$

and

$$\rho_v v_v(r,y=h,\theta)=\rho_l v_l^b(r,y=h,\theta)=\begin{cases}-\rho_v v_1 & (0\leqslant r\leqslant\varphi R)\\ \rho_v v_2 & (\varphi R\leqslant r\leqslant R)\end{cases}. \tag{8}$$

The continuities of velocities and shear stresses at these interfaces yields

$$u_v(r,y=0,\theta)=u_l^b(r,y=0,\theta)=u_i^b(r,\theta) \tag{9}$$

$$u_v(r, y = h, \theta) = u_l^t(r, y = h, \theta) = u_i^t(r, \theta) \quad (10)$$

and

$$\mu_v \left.\frac{\partial u_v}{\partial y}\right|_{y=0} = \mu_l \left.\frac{\partial u_l^b}{\partial y}\right|_{y=0} \quad (11)$$

$$\mu_v \left.\frac{\partial u_v}{\partial y}\right|_{y=h} = \mu_l \left.\frac{\partial u_l^t}{\partial y}\right|_{y=h}, \quad (12)$$

where $u_i^b(r, \theta)$ and $u_i^t(r, \theta)$ are the radial velocity components at the liquid–vapor interfaces, $y = 0$ and $y = h$, respectively. In the above presentation ρ_v is the vapor density and ρ_l the liquid density, μ_v the dynamic viscosity of vapor, μ_l the dynamic viscosity of the liquid, K and ε are the permeability and porosity of the top and bottom wicks, h the height of the vapor space, v_1 the vapor injection velocity and v_2 the vapor suction velocity. In equations (4) and (6), the geometric function F is calculated using the expression obtained in Vafai [8] ($F = 1.75/\sqrt{150\varepsilon^{3/2}}$). The momentum jump condition in the normal direction is not applied at the liquid–vapor interface since it is accounted for in the calculation of the capillary limit. Here, we have followed the very prominent approach in the heat pipe research up to date in which the vapor and liquid pressures are obtained independently and then combined with the Laplace–Young equation to yield an expression for the capillary limit. As indicated in equations (7) and (8), within the $0 \leqslant r \leqslant \varphi R$ region, the top wick acts as the evaporator and the bottom wick as the condenser. However, both top and bottom wicks act as condensers within the $\varphi R \leqslant r \leqslant R$ region.

The liquid flow within the top and bottom wicks are coupled through the liquid flow within the vertical wicks. Since the heat is removed from the top and bottom surface of the heat pipe and there is no heat sink to remove heat from the vertical wicks directly, the main role of the vertical wick is to transport liquid from the bottom wick to the top wick. Based on these conditions, vapor injection and suction on the vertical wicks as well as the radial liquid flow within the vertical wicks are neglected. Therefore, the mass conservation for the liquid within the vertical wicks yields

$$Q^b(r) = Q^t(r) = Q(r), \quad (13)$$

where

$$Q^b(r) = \int_{-h_w}^{0} (w_l^b(r, y, \theta = \Phi) - w_l^b(r, y, \theta = 0))\, dy \quad (14)$$

is the flow rate of liquid from the bottom wick to the vertical wicks at location r, and

$$Q^t(r) = -\int_{h_w}^{h+h} (w_l^t(r, y, \theta = \Phi) - w_l^t(r, y, \theta = 0))\, dy \quad (15)$$

is the flow rate of liquid from the vertical wicks to the top wick at location r. The parameter Φ in equations (14) and (15) is the angle of the vapor space for any one of the vapor flow channels, and h_w is the thickness of the top and bottom wicks. For the horizontal heat pipe under study, the liquid flow within the vertical wicks is based on Darcy's law, i.e.

$$Q(r) = -\frac{K_v h_{wv}}{\mu_l}\left(\frac{p_l^t(r) - p_l^b(r)}{h} + \rho_l g\right), \quad (16)$$

where $p_l^t(r)$, $p_l^b(r)$ denote the liquid pressure in the top and bottom wicks, respectively, K_v and h_{wv} are permeability and thickness of the vertical wick and g is the gravitational acceleration.

The boundary conditions are as follows:

$$\theta = 0: \quad u_v = 0 \quad u_l^b = 0 \quad u_l^t = 0 \quad (17)$$

$$\theta = \Phi: \quad u_v = 0 \quad u_l^b = 0 \quad u_l^t = 0 \quad (18)$$

$$y = -h_w: \quad u_l^b = 0 \quad v_l^b = 0 \quad (19)$$

$$y = h + h_w: \quad u_l^t = 0 \quad v_l^t = 0 \quad (20)$$

$$r = 0: \quad u_v = 0 \quad u_l^b = 0 \quad u_l^t = 0 \quad (21)$$

$$r = R: \quad u_v = 0 \quad u_l^b = 0 \quad u_l^t = 0, \quad p_v = p_l^b. \quad (22)$$

The above governing, boundary and coupling equations provide all necessary relations to obtain a closed mathematical solution. An in-depth integral method is employed to obtain the analytical solution for the vapor and liquid velocity profiles and pressure distributions.

1. *Vapor velocity profile*

A parabolic velocity profile is used for vapor flow within the heat pipe and is represented by a functional product in the r, y and θ directions, that is

$$u_v(r, y, \theta) = U_v(r)(a_0 + a_1 y + a_2 y^2)(c_0 + c_1\theta + c_2\theta^2). \quad (23)$$

Based on the continuity of velocity fields, the interfacial velocities are represented by functional products in the r and θ directions as follows:

$$u_i^b(r, \theta) = U_i^b(r)(c_0 + c_1\theta + c_2\theta^2) \quad (24)$$

and

$$u_i^t(r, \theta) = U_i^t(r)(c_0 + c_1\theta + c_2\theta^2), \quad (25)$$

where $U_v(r)$, $U_i^b(r)$ and $U_i^t(r)$ denote the maximum velocity for $u_v(r, y, \theta)$, $u_i^b(r, \theta)$ and $u_i^t(r, \theta)$ on every transverse surface along the r direction, respectively. Using the boundary conditions given by equations (17) and (18), the constants c_0, c_1 and c_2 for the θ component of $u_v(r, y, \theta)$, $u_i^b(r, \theta)$ and $u_i^t(r, \theta)$ can easily

be determined as follows:

$$c_0+c_1\theta+c_2\theta^2=\frac{4\theta}{\Phi}\left(1-\frac{\theta}{\Phi}\right). \tag{26}$$

It should be noted that the present analysis could be further extended to include vapor flow reversal by using a higher order polynomial. Due to the vapor injection from the heating side of the top wick, the location of the maximum vapor velocity $U_v(r)$ will be shifted towards the bottom wick within the $0 \leqslant r \leqslant \varphi R$ region. As the vapor flows downstream, the location of $U_v(r)$ will gradually shift towards the center line ($y = h/2$) due to the presence of symmetrical cooling conditions. To account for this feature, the vapor velocity profile in y direction is divided into two parts based on the location of the maximum vapor velocity: the lower part ($0 \leqslant y \leqslant f(r)$) and the upper part ($f(r) \leqslant y \leqslant h$). The location of the maximum vapor velocity, $y = f(r)$, is also the location corresponding to zero shear stress for the velocity distribution on the r–y plane. Applying the interfacial boundary conditions given by equations (9) and (10) as well as

$$u_v\left(r,y=f(r),\quad \theta=\frac{\Phi}{2}\right)=U_v(r),\quad \left.\frac{\partial u_v}{\partial y}\right|_{y=f(r)}=0 \tag{27}$$

to equation (23) results in the following vapor velocity profile

$$u_v(r,y,\theta)=\begin{cases}\left\{u_i^b(r)+[U_v(r)-u_i^b(r)]\left[2\dfrac{y}{f(r)}-\left(\dfrac{y}{f(r)}\right)^2\right]\right\}\dfrac{4\theta}{\Phi}\left(1-\dfrac{\theta}{\Phi}\right) & (0\leqslant y\leqslant f(r))\\ \left\{u_i^t(r)+[U_v(r)-u_i^t(r)]\left[2\dfrac{h-y}{h-f(r)}-\left(\dfrac{h-y}{h-f(r)}\right)^2\right]\right\}\dfrac{4\theta}{\Phi}\left(1-\dfrac{\theta}{\Phi}\right) & (f(r)\leqslant y\leqslant h).\end{cases} \tag{28}$$

2. *Liquid velocity profiles*

Utilizing the boundary conditions given by equations (17) and (18), the liquid velocity component in the r-direction can be taken as follows:

$$u_l^b(r,y,\theta)=u_l^b(r,y)\frac{4\theta}{\Phi}\left(1-\frac{\theta}{\Phi}\right) \tag{29}$$

$$u_l^t(r,y,\theta)=u_l^t(r,y)\frac{4\theta}{\Phi}\left(1-\frac{\theta}{\Phi}\right). \tag{30}$$

Vafai and Thiyagaraja [9] have shown that the thickness of the interface region between a porous medium and a fluid or an impermeable medium is of the order of $(K/\varepsilon)^{1/2}$. According to their investigation of the interface interactions in a saturated porous medium, the liquid velocity profile in the top and bottom wicks can be represented by three parts: an inner solution for the interface zone between the liquid–wick and the vapor phase, an outer solution for the main wick region and an inner solution for the interface zone between the liquid–wick and the heat pipe wall. Based on the matched asymptotic solution of Vafai and Thiyagaraja [9], and applying the boundary conditions given by equations (9) and (19) and noticing that the thickness of the interface regions is much smaller than $h_w/2$ for the heat pipe under study, the following velocity profile is obtained for the liquid flow within the bottom wick ($-h_w \leqslant y \leqslant 0$):

$$u_l^b(r,y)=\begin{cases}U_l^b(r)+[U_i^b(r)-U_l^b(r)]\exp\left(\dfrac{y}{\sqrt{K/\varepsilon}}\right) & -\dfrac{h_w}{2}\leqslant y\leqslant 0\\ U_l^b(r)\left[1-\exp\left(-\dfrac{h_w+y}{\sqrt{K/\varepsilon}}\right)\right] & -h_w\leqslant y\leqslant -\dfrac{h_w}{2}.\end{cases} \tag{31}$$

Similarly, for the liquid flow within the top wick, we have

$$u_l^t(r,y)=\begin{cases}U_l^t(r)+[U_i^t(r)-U_l^t(r)]\exp\left(-\dfrac{y-h}{\sqrt{K/\varepsilon}}\right) & h\leqslant y\leqslant h+\dfrac{h_w}{2}\\ U_l^t(r)\left[1-\exp\left(\dfrac{y-(h+h_w)}{\sqrt{K/\varepsilon}}\right)\right] & h+\dfrac{h_w}{2}\leqslant y\leqslant h+h_w.\end{cases} \tag{32}$$

The maximum interfacial radial velocity components are determined by matching the interfacing shear stresses given in equations (11) and (12). This results in

$$U_i^b(r)=\frac{U_v(r)+\dfrac{\gamma\mu^+ f(r)}{2}U_l^b(r)}{1+\dfrac{\gamma\mu^+ f(r)}{2}} \tag{33}$$

and

$$U_i^{\mathrm{t}}(r)=\frac{U_{\mathrm{v}}(r)+\dfrac{\gamma\mu^{+}(h-f(r))}{2}U_1^{\mathrm{t}}(r)}{1+\dfrac{\gamma\mu^{+}(h-f(r))}{2}}, \tag{34}$$

where $\mu^{+}=\mu_1/\mu_{\mathrm{v}}$, and $\gamma=\sqrt{\varepsilon/K}$ is the shape parameter of the top and bottom porous wicks.

3. *The maximum radial velocity component of vapor and liquid flows*

The maximum vapor and liquid radial velocity components $U_{\mathrm{v}}(r)$, $U_1^{\mathrm{b}}(r)$ and $U_1^{\mathrm{t}}(r)$ are determined by integrating the vapor and liquid continuity equations. Utilizing the velocity profiles and boundary conditions given by equations (28), (24), (25), (7) and (8), the integration of the continuity equation (1) with respect to y from 0 to h and with respect to θ from 0 to Φ yields

$$U_i^{\mathrm{b}}(r)f(r)+U_i^{\mathrm{t}}(r)(h-f(r))+2hU_{\mathrm{v}}(r)=\begin{cases}\dfrac{9(v_1-v_2)}{4}r & (0\leqslant r\leqslant\varphi R)\\ \dfrac{9v_2}{2}\dfrac{R^2-r^2}{r} & (\varphi R\leqslant r\leqslant R).\end{cases} \tag{35}$$

For the liquid flow within the bottom wick, integrating the continuity equation (3) with respect to y from $-h_{\mathrm{w}}$ to 0 and with respect to θ from 0 to Φ and substituting the velocity profiles and boundary conditions given by equations (29), (31), (33), (13), (14), (16), (7) and (19) results in the following expression for $U_1^{\mathrm{b}}(r)$:

$$U_1^{\mathrm{b}}(r)=\frac{3v_2}{4\rho^{+}h_{\mathrm{w}}}r-\frac{3K_{\mathrm{v}}h_{\mathrm{wv}}}{2\Phi\mu_1hh_{\mathrm{w}}r}\int_0^r(p_1^{\mathrm{b}}(r)-p_1^{\mathrm{t}}(r)-\rho_1gh)\,\mathrm{d}r-\frac{2U_{\mathrm{v}}(r)}{\gamma^2\mu^{+}h_{\mathrm{w}}f(r)}, \tag{36}$$

where $\rho^{+}=\rho_1/\rho_{\mathrm{v}}$. To obtain equation (36), the simplification $1+\frac{1}{2}\gamma\mu^{+}f(r)\approx\frac{1}{2}\gamma\mu^{+}f(r)$ is utilized based on the fact that $\mu^{+}f(r)$ is at least of the order of h_{w}. For the liquid flow within the top wick, integrating the continuity equation (5) with respect to y from h to $h+h_{\mathrm{w}}$ and with respect to θ from 0 to Φ and substituting the corresponding velocity profiles and boundary conditions results in the following expression for $U_1^{\mathrm{t}}(r)$

$$U_1^{\mathrm{t}}(r)=\begin{cases}-\dfrac{3v_1}{4\rho^{+}h_{\mathrm{w}}}r+\dfrac{3K_{\mathrm{v}}h_{\mathrm{wv}}}{2\Phi\mu_1hh_{\mathrm{w}}r}\displaystyle\int_0^r(p_1^{\mathrm{b}}(r)-p_1^{\mathrm{t}}(r)-\rho_1gh)\,\mathrm{d}r-\frac{2U_{\mathrm{v}}}{\gamma^2\mu^{+}h_{\mathrm{w}}(h-f(r))} & (0\leqslant r\leqslant\varphi R)\\ \dfrac{3v_2}{4\rho^{+}h_{\mathrm{w}}}\dfrac{r^2-2R^2}{r}+\dfrac{3K_{\mathrm{v}}h_{\mathrm{wv}}}{2\Phi\mu_1hh_{\mathrm{w}}r}\displaystyle\int_0^r(p_1^{\mathrm{b}}(r)-p_1^{\mathrm{t}}(r)-\rho_1gh)\,\mathrm{d}r-\frac{2U_{\mathrm{v}}}{\gamma^2\mu^{+}h_{\mathrm{w}}(h-f(r))} & (\varphi R\leqslant r\leqslant R).\end{cases} \tag{37}$$

Substituting equations (36) and (37) into equations (33) and (34) results in the following expressions for $U_i^{\mathrm{b}}(r)$ and $U_i^{\mathrm{t}}(r)$:

$$U_i^{\mathrm{b}}(r)=\frac{3v_2}{4\rho^{+}h_{\mathrm{w}}}r-\frac{3K_{\mathrm{v}}h_{\mathrm{wv}}}{2\Phi\mu_1hh_{\mathrm{w}}r}\int_0^r(p_1^{\mathrm{b}}(r)-p_1^{\mathrm{t}}(r)-\rho_1gh)\,\mathrm{d}r+\frac{2U_{\mathrm{v}}(r)}{\gamma\mu^{+}f(r)} \tag{38}$$

and

$$U_i^{\mathrm{t}}(r)=\begin{cases}-\dfrac{3v_1}{4\rho^{+}h_{\mathrm{w}}}r+\dfrac{3K_{\mathrm{v}}h_{\mathrm{wv}}}{2\Phi\mu_1hh_{\mathrm{w}}r}\displaystyle\int_0^r(p_1^{\mathrm{b}}(r)-p_1^{\mathrm{t}}(r)-\rho_1gh)\,\mathrm{d}r+\frac{2U_{\mathrm{v}}}{\gamma\mu^{+}(h-f(r))} & (0\leqslant r\leqslant\varphi R)\\ \dfrac{3v_2}{4\rho^{+}h_{\mathrm{w}}}\dfrac{r^2-2R^2}{r}+\dfrac{3K_{\mathrm{v}}h_{\mathrm{wv}}}{2\Phi\mu_1hh_{\mathrm{w}}r}\displaystyle\int_0^r(p_1^{\mathrm{b}}(r)-p_1^{\mathrm{t}}(r)-\rho_1gh)\,\mathrm{d}r+\frac{2U_{\mathrm{v}}}{\gamma\mu^{+}(h-f(r))} & (\varphi R\leqslant r\leqslant R).\end{cases} \tag{39}$$

Substituting equations (38) and (39) into equation (35) results in the following expressions for $U_{\mathrm{v}}(r)$

$$U_{\mathrm{v}}(r)=\begin{cases}\dfrac{9(v_1-v_2)}{8h}r+\dfrac{3r}{8\rho^{+}hh_{\mathrm{w}}}(v_1(h-f(r))-v_2f(r))-\dfrac{3K_{\mathrm{v}}h_{\mathrm{wv}}(h-2f(r))}{4\Phi\mu_1h^2h_{\mathrm{w}}r}\displaystyle\int_0^r(p_1^{\mathrm{b}}(r)-p_1^{\mathrm{t}}(r)-\rho_1gh)\,\mathrm{d}r & (0\leqslant r\leqslant\varphi R)\\ \dfrac{9v_2}{4h}\dfrac{R^2-r^2}{r}-\dfrac{3v_2}{8\rho^{+}hh_{\mathrm{w}}r}(hr^2-2(h-f(r))R^2)-\dfrac{3K_{\mathrm{v}}h_{\mathrm{wv}}(h-2f(r))}{4\Phi\mu_1h^2h_{\mathrm{w}}r}\displaystyle\int_0^r(p_1^{\mathrm{b}}(r)-p_1^{\mathrm{t}}(r)-\rho_1gh)\,\mathrm{d}r & (\varphi R\leqslant r\leqslant R).\end{cases} \tag{40}$$

The continuity of $U_v(r)$, $U_l^1(r)$ and $U_l^2(r)$ at $r = \varphi R$ all leads to the following consistent relationship

$$\varphi = \sqrt{\frac{2v_2}{v_1+v_2}}. \tag{41}$$

4. *The location of the maximum vapor velocity*

The location of the maximum vapor velocity, $f(r)$, is determined by integrating the vapor momentum equation (2) with respect to y from 0 to $f(r)$ and with respect to θ from 0 to Φ. Since the dimension in r-direction is much larger than the transverse length in the vapor channel, the shear stress in r-direction is neglected [10]. It should also be noted that in the $0 \leqslant r \leqslant \varphi R$ region of the vapor passage, there is a mass flow crossing $y = f(r)$ surface in the y-direction due to the vapor injection from the top wick and suction from the bottom wick. However, there is no mass flow crossing $y = f(r)$ surface in the $\varphi R \leqslant r \leqslant R$ region due to symmetrical boundary conditions on both top and bottom wicks. Based on the above considerations, the integration of the momentum equation (2) using the vapor velocity profile and the average vapor pressure in each transverse plane results in the following expression for the rate of change of $f(r)$

$$\frac{df(r)}{dr} = \begin{cases} \dfrac{1}{D(r)}\left\{-\dfrac{2}{h}(2G(r)+3U_v(r))\left(\dfrac{dG(r)}{dr}+\dfrac{3(v_1-v_2)}{8\rho^+h_w}\right)f^2(r)+\left[2(4G(r)+U_v(r))\dfrac{dG(r)}{dr}\right.\right. \\ \quad +\dfrac{3(v_1-v_2)}{4h}\left(3+\dfrac{h}{\rho^+h_w}\right)(2G(r)+3U_v(r))+\dfrac{1}{r}(3G^2(r)-G(r)U_v(r)-2U_v^2(r)) \\ \quad \left.\left.+\dfrac{75\mu_v}{\rho_v\Phi^2r^2}(G(r)+2U_v(r))+\dfrac{225}{8\rho_v}\dfrac{dp_v}{dr}\right]f(r)-\dfrac{75}{4}\left(\dfrac{2\mu_v}{\rho_v f(r)}-v_2\right)(G(r)-U_v(r))\right\} \\ \qquad\qquad (0 \leqslant r \leqslant \varphi R) \\ \dfrac{1}{D(r)}\left\{-\dfrac{4G(r)}{h}\left(\dfrac{dG(r)}{dr}-\dfrac{3v_2}{4\rho^+h_w}\dfrac{R^2+r^2}{r^2}\right)f^2(r)+\left[4(2G(r)+U_v(r))\dfrac{dG(r)}{dr}\right.\right. \\ \quad -\dfrac{3v_2}{h}\left(3+\dfrac{h}{\rho^+h_w}\right)\dfrac{R^2+r^2}{r^2}G(r)+\dfrac{1}{r}(3G^2(r)+4G(r)U_v(r)+8U_v^2(r)) \\ \quad \left.\left.+\dfrac{75\mu_v}{\rho_v\Phi^2r^2}(G(r)+2U_v(r))+\dfrac{225}{8\rho_v}\dfrac{dp_v}{dr}\right]f(r)-\dfrac{75\mu_v}{2\rho_v}\dfrac{G(r)-U_v(r)}{f(r)}\right. \\ \quad \left.+\dfrac{75v_2}{4}\left(G(r)+\dfrac{2U_v(r)}{\gamma\mu^+f(r)}\right)\right. \qquad (\varphi R \leqslant r \leqslant R), \end{cases} \tag{42}$$

where

$$G(r) = \frac{3v_2}{4\rho^+h_w}r - \frac{3K_vh_{wv}}{2\Phi\mu_lhh_wr}\int_0^r (p_l^b(r)-p_l^1(r)-\rho_lgh)\,dr \tag{43}$$

and

$$D(r) = \begin{cases} 2U_v^2(r)+\left[\left(1+\dfrac{6f(r)}{h}+\dfrac{12}{\gamma\mu^+f(r)}\right)G(r)+\dfrac{9(v_1-v_2)r}{4\rho^+hh_w}f(r)\right]U_v(r) \\ \quad -\left[\left(3-\dfrac{4f(r)}{h}\right)G(r)-\dfrac{3(v_1-v_2)r}{2\rho^+hh_w}f(r)\right]G(r) \\ \qquad\qquad (0 \leqslant r \leqslant \varphi R) \\ 7U_v^2(r)-4G(r)U_v(r)-\left(3-\dfrac{4f(r)}{h}\right)G^2(r)+\dfrac{3v_2f(r)}{\rho^+hh_w}\dfrac{R^2-r^2}{r}G(r) \\ \qquad\qquad (\varphi R \leqslant r \leqslant R). \end{cases} \tag{44}$$

5. *Vapor and liquid pressure distributions*

The pressure distribution in the vapor phase can be obtained by integrating r-momentum equation (2) within a vapor channel bounded by porous wicks. Introducing continuity equation (1), vapor velocity profile given by equation (28) and boundary conditions given by equations (7)–(10), (17) and (18) as well as equations (24), (25), (27) and (35) into the integrated momentum equation results in the following expression for the vapor pressure gradient:

$$\frac{dp_v}{dr}=\begin{cases}-\dfrac{8\rho_v}{75hr}\dfrac{d}{dr}\{r[(U_i^b(r))^2f(r)+(U_i^t(r))^2(h-f(r))+3(v_1-v_2)rU_v(r)]\}\\ \quad-\dfrac{4\mu_v}{3hf(r)(h-f(r))}\left[\dfrac{9(v_1-v_2)}{4}r-(U_i^b(r)+U_i^t(r)+U_v(r))h\right]\\ \quad+\dfrac{2\rho_v}{3h}(v_1U_i^t(r)-v_2U_i^b(r))-\dfrac{6\mu_v(v_1-v_2)}{\Phi^2hr} & (0\leqslant r\leqslant\varphi R)\\ -\dfrac{8\rho_v}{75hr}\dfrac{d}{dr}\left\{r\left[(U_i^b(r))^2f(r)+(U_i^t(r))^2(h-f(r))+6v_2\dfrac{R^2-r^2}{r}U_v(r)\right]\right\}\\ -\dfrac{2\mu_v}{3hf(r)(h-f(r))}\left[9v_2\dfrac{R^2-r^2}{r}-2(U_i^b(r)+U_i^t(r)+U_v(r))h\right]\\ -\dfrac{2\rho_vv_2}{3h}(U_i^b(r)+U_i^t(r))-\dfrac{12\mu_vv_2}{\Phi^2h}\dfrac{R^2-r^2}{r^3} & (\varphi R\leqslant r\leqslant R).\end{cases}\tag{45}$$

The liquid pressure distributions are determined by integrating the generalized momentum equations (4) and (6) within the top and bottom wicks, respectively. The shear stress in the r-direction is neglected, since the dimension in r-direction is much larger than the transvesrse length in the channel. For the bottom wick, integrating equation (4) with velocity profile given by equations (29) and (31), boundary conditions given by equations (7), (9), (17)–(19) as well as equations (24) and (25) results in the following expression for the liquid pressure gradient within the bottom wick:

$$\frac{dp_l^b}{dr}=-\frac{2\mu_l}{3K}U_l^b(r)-\frac{8\mu_l}{\varepsilon\Phi^2r^2}\left(U_l^b(r)+\frac{U_i^b(r)}{\gamma h_w}\right)+\frac{8\rho_lF\varepsilon}{15K^{1/2}}\left[U_l^b(r)\left(U_l^b(r)+\frac{U_i^b(r)}{\gamma h_w}\right)+\frac{(U_i^b(r))^2}{2\gamma h_w}\right].\tag{46}$$

Similarly, the integration of equation (6) with corresponding velocity profile and boundary conditions results in the following expression for the liquid pressure gradient within the top wick:

$$\frac{dp_l^t}{dr}=-\frac{2\mu_l}{3K}U_l^t(r)-\frac{8\mu_l}{\varepsilon\Phi^2r^2}\left(U_l^t(r)+\frac{U_i^t(r)}{\gamma h_w}\right)+\frac{8\rho_lF\varepsilon}{15K^{1/2}}\left[U_l^t(r)\left(U_l^t(r)+\frac{U_i^t(r)}{\gamma h_w}\right)+\frac{(U_i^t(r))^2}{2\gamma h_w}\right].\tag{47}$$

6. *The liquid–vapor interface temperature*

The temperature along the liquid–vapor interface is taken as the saturation temperature corresponding to the vapor pressure at the interface. Since the parabolic version of the equations of motion is used in the current model, the vertical variation of the vapor pressure is not accounted for. Based on the Clausius–Clapeyron equation, the interface temperature can be found from

$$T_v(r)=\frac{T_v(0)}{1-T_v(0)\bar{R}[\ln p_v(r)-\ln p_v(0)]/h_{fg}},\tag{48}$$

where $\bar{R}$ is the ideal gas constant and h_{fg} is the latent heat of working fluid.

7. *The maximum heat transport capillary limit*

For a heat pipe under steady-state operation, stable circulation of the working fluid in the heat pipe is achieved through the capillary pressure established by the wick structure. If a heat pipe is to operate continuously without drying out the wick, the sum of the pressure losses along the vapor–liquid path for each wall should not exceed the maximum possible capillary pressure for that wall; that is

$$\frac{2\sigma_l}{r_c}\geqslant\Delta p_v(r_{max}-r_{min})+\Delta p_l(r_{min}-r_{max})+p_c(r_{min}),\tag{49}$$

where $p_c(r_{min})=p_v(r_{min})-p_l(r_{min})$ is the minimum capillary pressure, σ_l is the surface tension of the liquid, r_c denotes the effective pore radius of the top

and bottom wicks, and r_{max}/r_{min} denotes the location where the capillary pressure is maximum/minimum. The notation $\Delta p(r_{max}-r_{min})$ means that Δp is evaluated over the distance $(r_{max}-r_{min})$. For the disk-shaped heat pipe under current study, which is heated from the top surface, the entire bottom wick acts only as the condenser and the overall liquid pressure drop within the bottom wick is always smaller than that within the top wick, due to the coupling of the liquid flows in the top and bottom wicks through the vertical wicks. Therefore, the sum of the pressure losses along the vapor–liquid path for the bottom wall is always smaller than that for the top wall. If the same porous wick structures are taken for both top and bottom wicks, the maximum heat transfer attainable in the heat pipe is achieved when the sum of the pressure losses along the vapor–liquid path for the top wall is equal to the maximum possible capillary pressure, i.e.

$$\frac{2\sigma_l}{r_c} \geqslant \Delta p_v^t(r_{max}-r_{min}) + \Delta p_l^t(r_{min}-r_{max}) + p_c^t(r_{min}). \tag{50}$$

RESULTS AND DISCUSSION

Nine unknowns in equations (36)–(40), (42) and (45)–(47), namely U_l^b, U_l^t, U_i^b, U_i^t, U_v, $f(r)$, p_v, p_l^b and p_l^t, are variables depending on r. To solve the above nine equations for the unknowns, equations (46) and (47) are combined to obtain an ordinary differential equation for $p_l^b(r)-p_l^t(r)$, subject to the following boundary conditions:

$$r = R, \quad p_l^b - p_l^t = \rho_l g h \tag{51}$$

and

$$\int_0^R [p_l^b(r) - p_l^t(r) - \rho_l g h]\,dr = \frac{\mu_l \Phi R^2 h v_2}{2\rho^+ K_v h_{wv}}. \tag{52}$$

The boundary condition (51) is obtained from equation (16) with no mass exchange through the vertical wicks at $r = R$, while equation (52) is obtained through the balance of the rate of vapor mass condensed on the bottom wick and the rate of liquid mass transferred from the bottom wick to the top wick at steady state. The ordinary differential equation for $p_l^b(r)-p_l^t(r)$ and equations (36)–(40), (42) and (45) are solved simultaneously as a function of the input heat power. The fourth-order Runge–Kutta method is used to solve the ordinary differential equations.

The results in Figs. 2–8 are based on a disk-shaped heat pipe with heavy water as the working fluid. The respective dimensions of the copper heat pipe are chosen as: $R = 0.25$ m, $\Phi = 45°$, $h = 0.0254$ m and $h_w = h_{wv} = 0.003$ m. The radius of the circular heat input zone is 0.125 m. The top and bottom wick material is copper foam; its effective pore radius, porosity and permeability are taken as 0.019 cm, 0.9 and 1.5×10^{-9} m^2, respectively. The vertical wick material is sintered copper powder; its effective pore radius, porosity and permeability are taken as 36 μm, 0.5 and 2.1×10^{-11} m^2, respectively. The results in Figs. 2–8 were obtained for the operating temperature of 80°C and for Re_h (injection Reynold's number, $Re_h = \rho_v v_l h/\mu_v$) values of 512, 1024 and 1536, which correspond to the input heat powers of 25, 50 and 75 kW, respectively. It should be noted that the primary purpose of this work is to study the effects of vapor–liquid hydrodynamic coupling and non-Darcian transport through the porous wick on predicting the heat pipe operation. The disk-shaped heat pipe was also simulated at low heat input power (1, 5 and 10 kW). Boiling cannot occur in the porous wick at these low heat loads. The results show the same tendency of the effects of vapor–liquid hydrodynamic coupling and non-Darcian transport as those presented in Figs. 2–8.

The variation of the maximum vapor velocity and its location, as well as the variation of the maximum liquid velocities and the interfacial velocities along the heat pipe, are shown in Figs. 2 and 3. The positive velocity value denotes that the flow is along r direction and the negative velocity value denotes that the flow is along the negative r direction. As can be seen from Fig. 2, vapor accelerates in the $0 \leqslant r \leqslant \varphi R$ region corresponding to the evaporator section and decelerates in the $\varphi R \leqslant r \leqslant R$ region corresponding to the condenser section, due to the vapor injection and suction over the corresponding regions. The location of the maximum vapor velocity is shifted down to the cooling side in the $0 \leqslant r \leqslant \varphi R$ region due to the injection from the heating side while it returns to the center line of the heat pipe in the $\varphi R \leqslant r \leqslant R$ region due to the symmetrical cooling conditions (Fig. 2b). The condensate in the top wick accelerates in the $\varphi R \leqslant r \leqslant R$ region and decelerates in the $0 \leqslant r \leqslant \varphi R$ region. At the condenser region close to the end of the heat pipe ($r = R$), there is no liquid exchange through the vertical wicks due to symmetrical cooling conditions and the liquid flow rates in the top and bottom wicks are the same. Starting at a certain location (around $r/R = 0.75$ in Fig. 3a), part of the condensate in the bottom wick is transferred to the top wick through the vertical wicks and leads to a larger liquid flow rate in the top wick.

This demonstrates that the assumption of the same flow rates in the top and bottom wicks is not suitable for the disk-shaped heat pipe heated from the top. An interesting phenomena is that the liquid may not necessarily decelerate to a zero velocity at $r = 0$. When the input heat is high enough, there is a region near $r = 0$ in the top wick within which the liquid flows in the same direction as the vapor flow. The liquid in this region is supplied by the bottom wick through the vertical wicks. The higher the input heat flux, the larger the liquid flow rate in the r-direction. There are two possible reasons that can cause this phenomena. One is that at high heat flux the vertical wicks cannot transfer enough liquid from the bottom wick to the

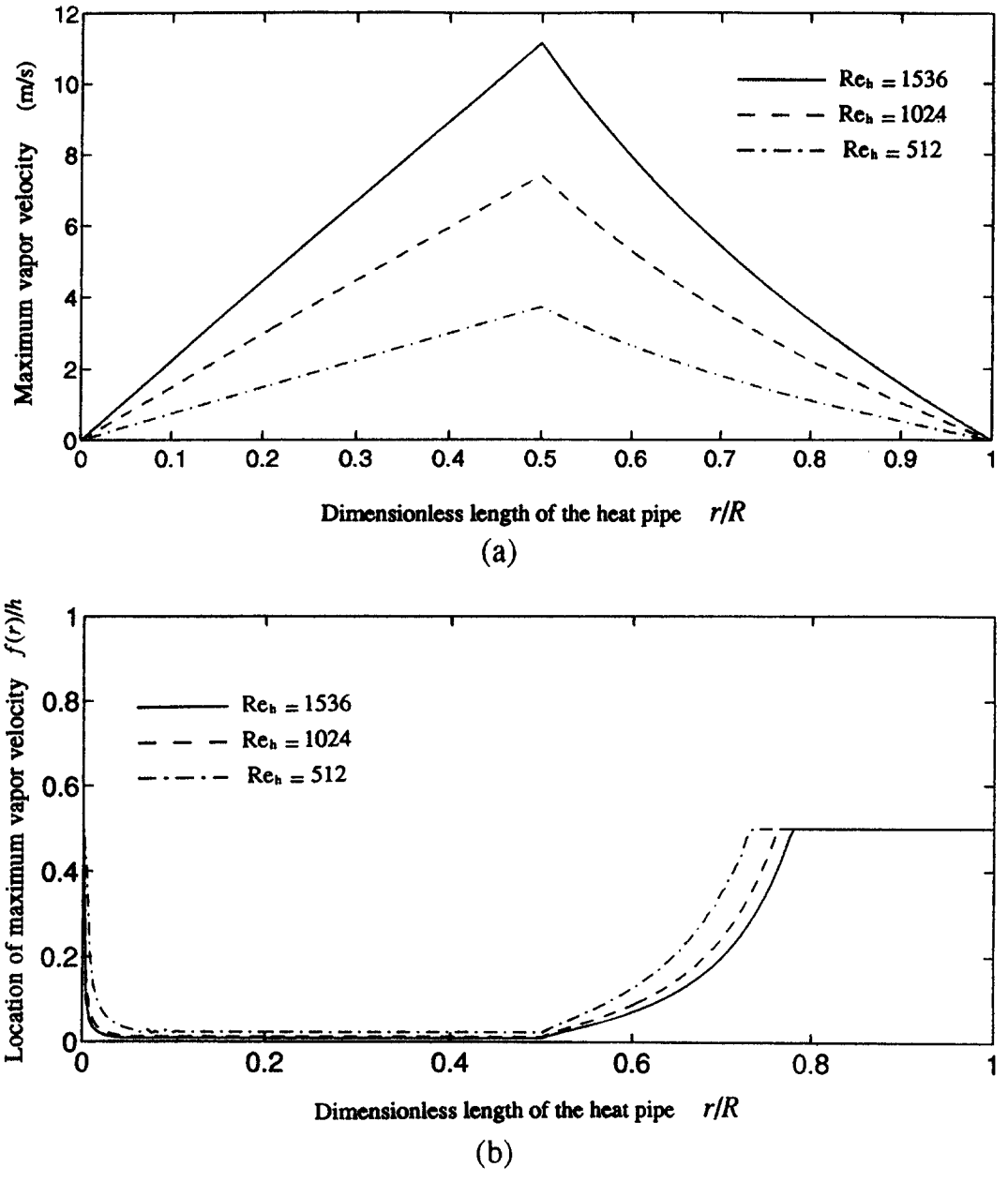

Fig. 2. Variations of the maximum vapor velocity and its location along the heat pipe.

top wick to keep the liquid flow within the top wick always in the negative r-direction. Our results have shown that the r-direction flow in the top wick is reduced, or eliminated, when a smaller permeability of the vertical wicks is taken, and the location where the mass exchange through the vertical wicks starts gets closer to $r = R$ for a smaller permeability of the vertical wicks. This is expected, since a smaller permeability results in a higher capillary pumping ability of the vertical wicks. The second possible reason is that the imposed heat flux exceeds the dry-out heat flux limit of the top wick, but the bottom wick still does not reach its capillary pumping limit, since the liquid flow rate in the bottom wick is smaller than that in the top wick, and supplies enough condensation to the dry-out region of the top wick through vertical wicks. Our results have also shown that both the flow rate and the region over which the liquid moves in the positive r-direction are reduced for smaller top wick permeabilities, while the thickness and permeability of the vertical wicks are kept fixed. This feature of directly feeding the evaporator with liquid from the bottom wick allows the disk-shaped heat pipe to obtain a higher heat flux capability than a conventional cylindrical heat pipe, which has only one path for the condensate return.

Figure 4 shows the vapor and liquid pressure distributions along the heat pipe. The vapor pressures in

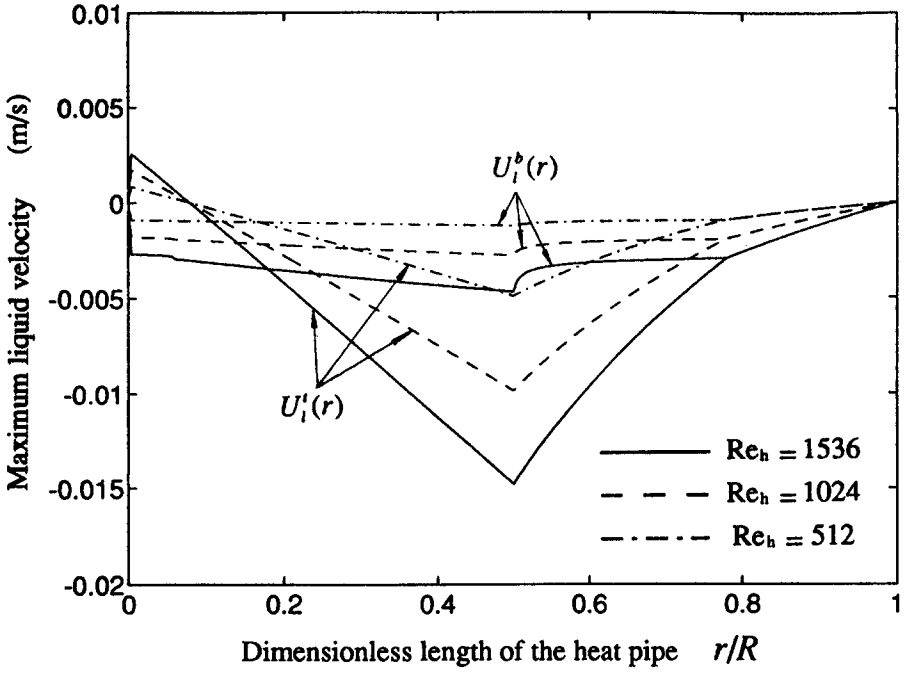

(a)

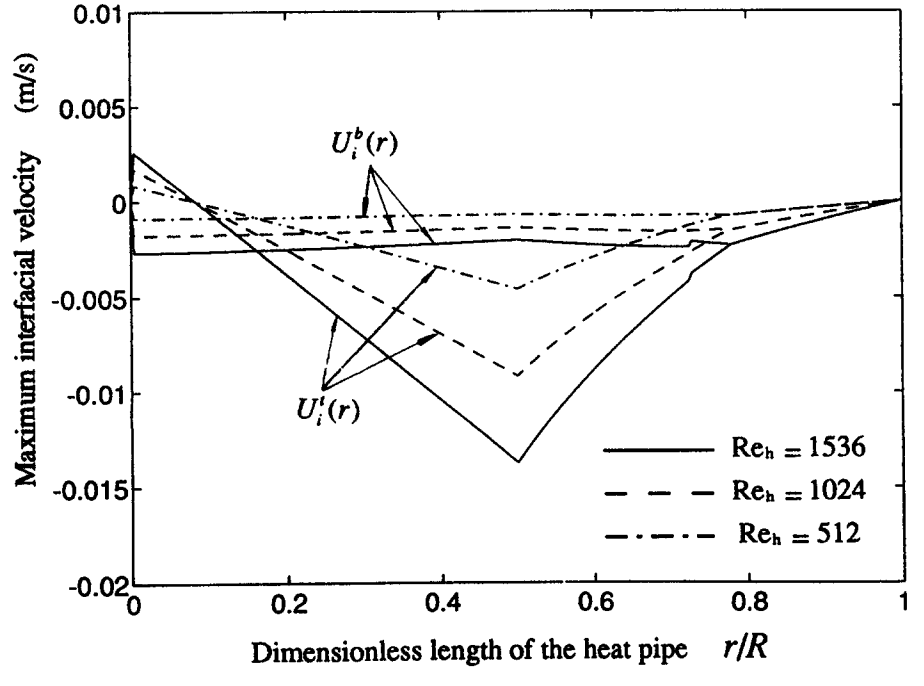

(b)

Fig. 3. Variations of maximum liquid velocity and maximum interfacial velocity along the heat pipe.

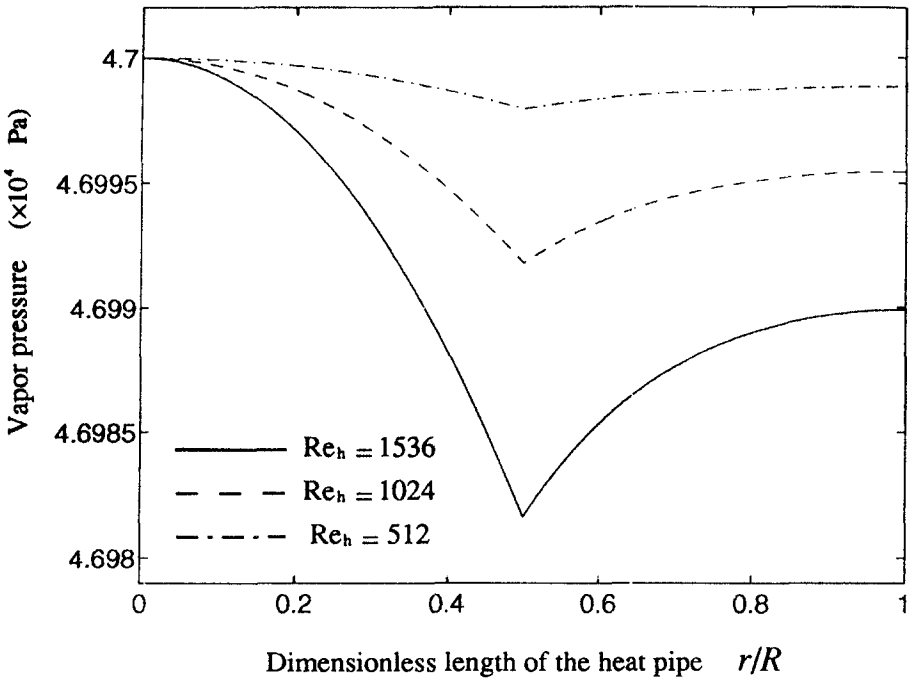

(a)

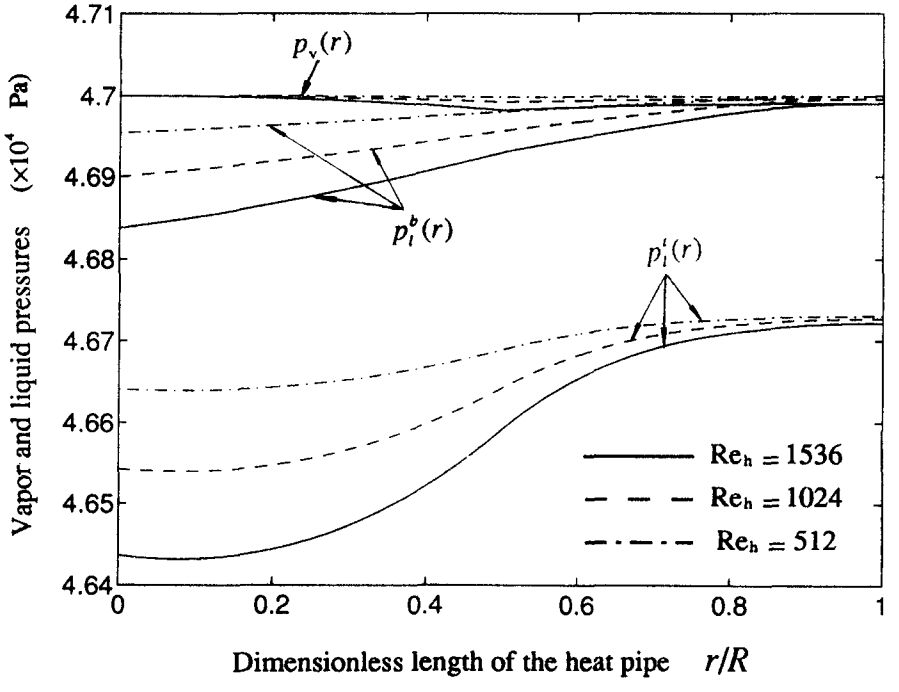

(b)

Fig. 4. Vapor and liquid pressure distributions along the heat pipe.

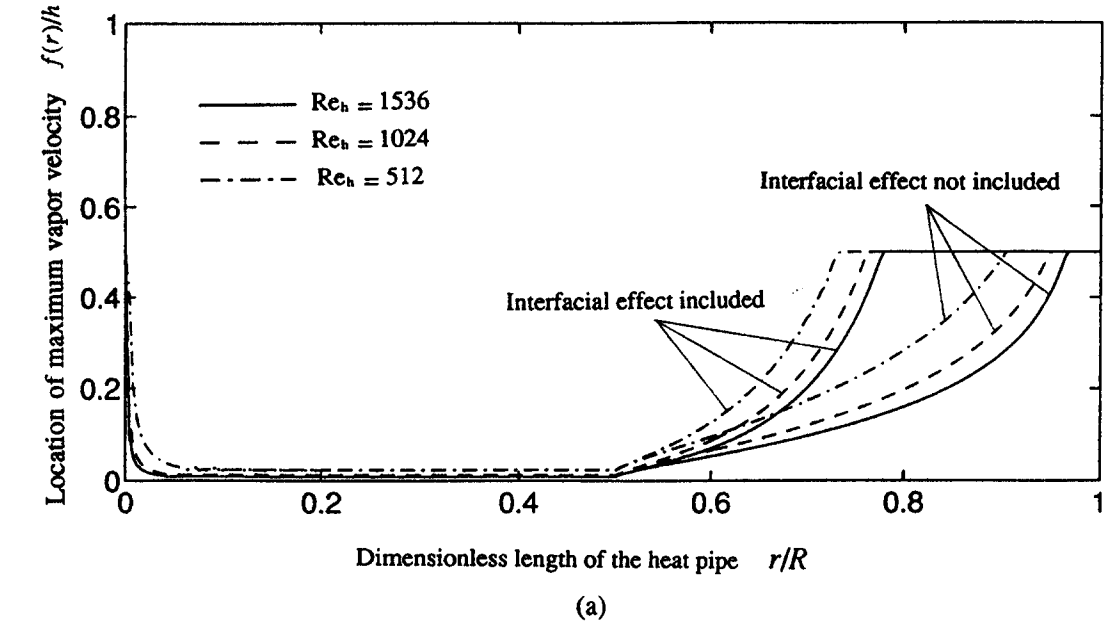

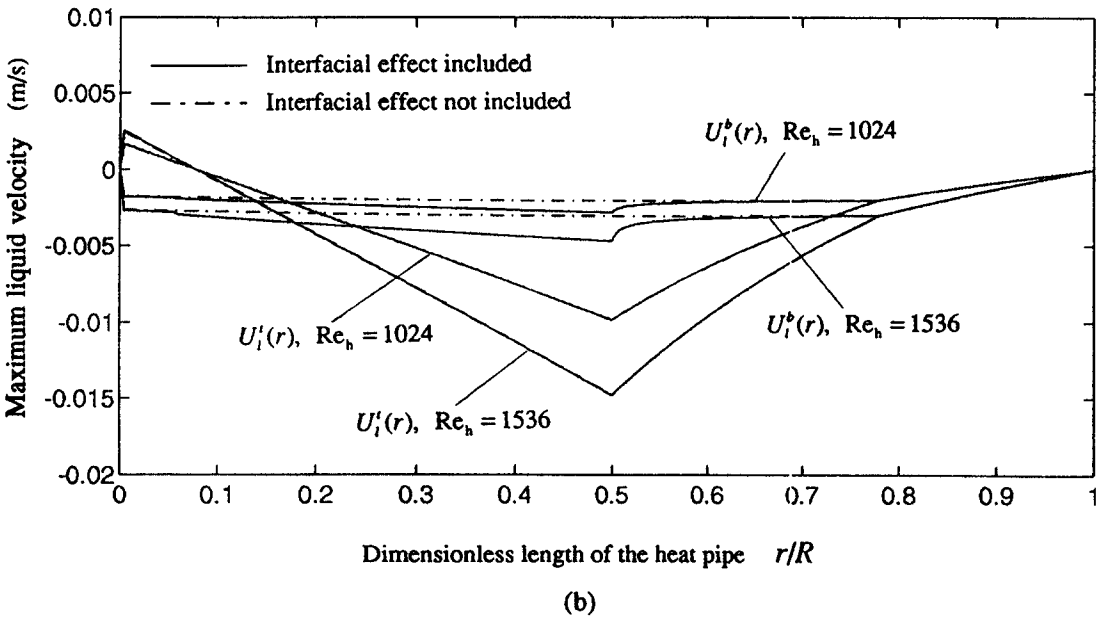

Fig. 5. The effect of vapor–liquid interfacial hydrodynamic coupling on (a) the location of the maximum vapor velocity, and (b) the maximum liquid velocities.

the $0 \leqslant r \leqslant \varphi R$ region decrease due to the friction and the acceleration of the vapor flow caused by mass injection from the top wick, while the vapor pressures in the $\varphi R \leqslant r \leqslant R$ region increase owing to the deceleration of the vapor flow by mass suction. The larger the injection Reynolds number, the larger the overall vapor pressure drop. Figure 4b shows that the liquid pressure in the top wick is always smaller than that in the bottom wick. In the region where no mass exchange through the vertical wicks occurs, the difference between the liquid pressures in the top and bottom wicks is only caused by the gravity, and is constant. In the region where the mass exchange through the vertical wicks occurs, this difference is caused not only by the gravity, but also by the frictional resistance for the liquid flow in the vertical wicks.

The effect of the vapor–liquid interfacial hydrodynamic coupling (the interfacial effect) on the vapor and liquid flows is illustrated in Figs. 5 and 6a. Our results show that the interfacial effect on the vapor flow rate is negligible. This is because the vapor flow

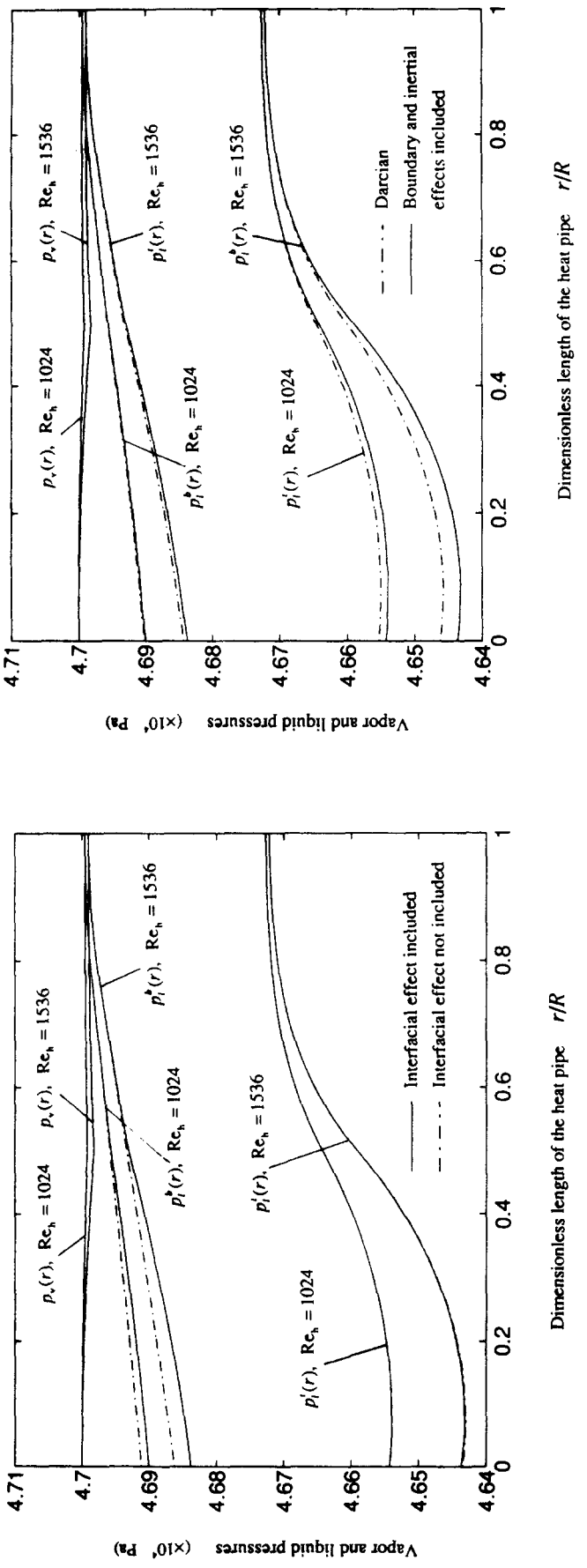

Fig. 6. The effects of (a) vapor–liquid interfacial hydrodynamic coupling, and (b) boundary and inertia on vapor and liquid pressures.

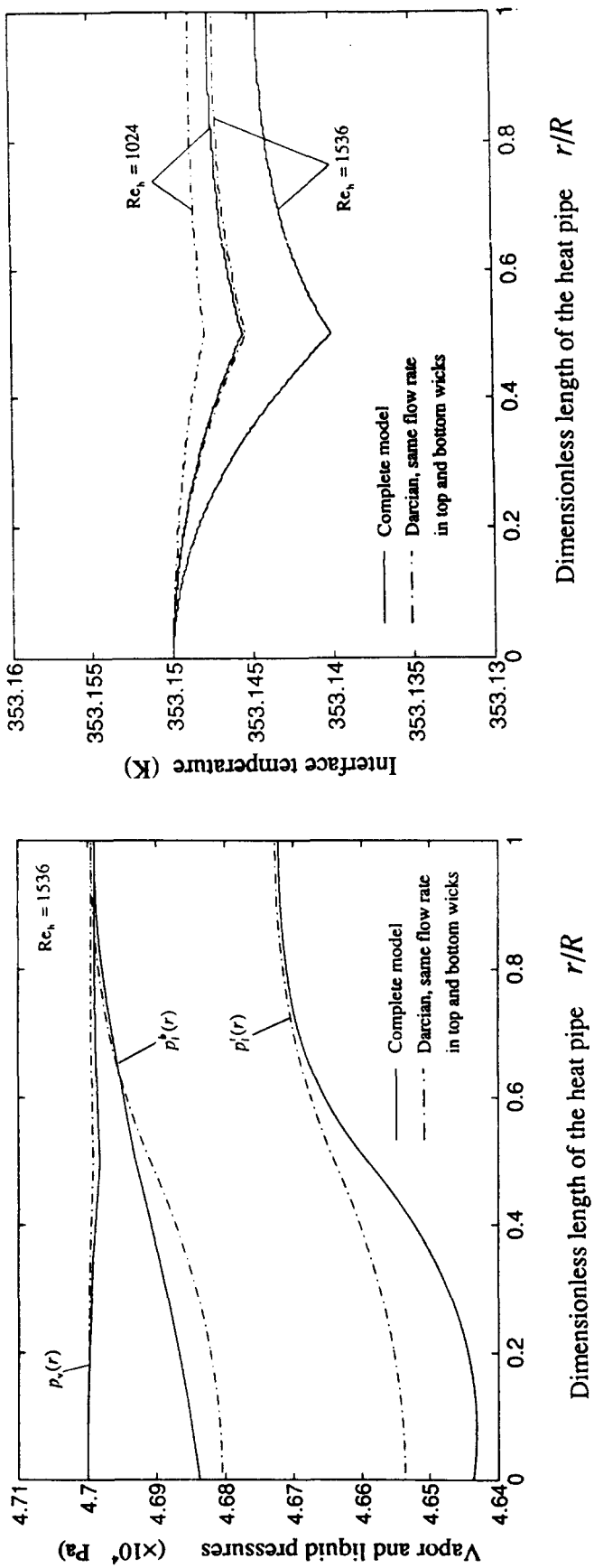

Fig. 7. Comparison of (a) vapor and liquid pressure distributions, and (b) vapor temperature distribution calculated with/without the assumption of same liquid flow rate within the top and bottom wicks.

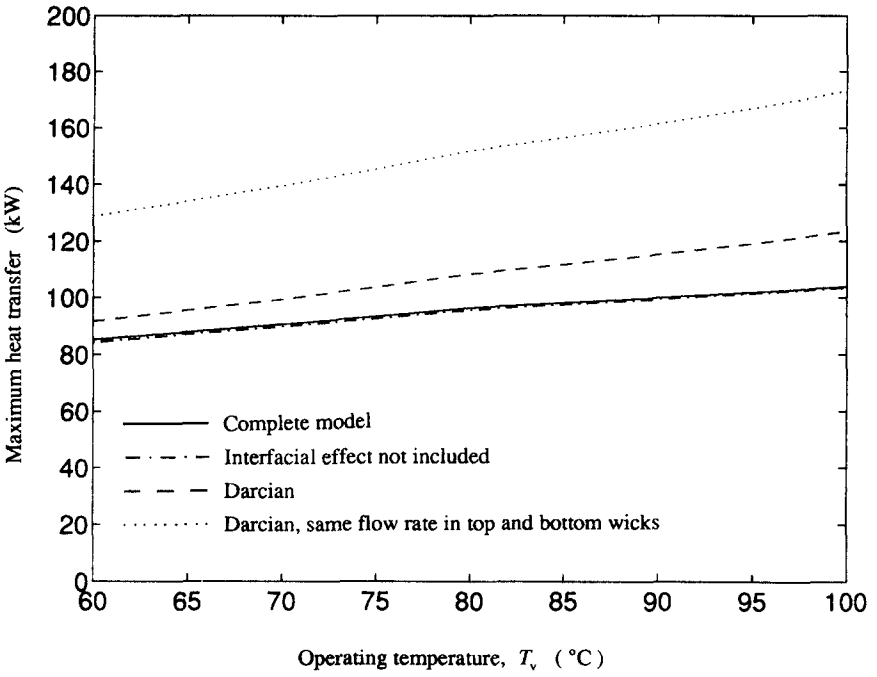

Fig. 8. The effects of vapor–liquid interfacial hydrodynamic coupling and boundary and inertia on the maximum heat transfer capability of the heat pipe.

rate is mainly determined by the vapor injection and suction velocities and is much larger than liquid flow rates. However, the interfacial effect on the location of the maximum vapor velocity is significant due to the shear stress at the vapor–liquid interface (Fig. 5a). Figure 5b shows the interfacial effect on the maximum liquid velocities. While the interfacial effect on the maximum liquid velocity in the top wick is negligible, it results in a larger maximum liquid velocity in the bottom wick. Figure 6a shows the interfacial effect on the vapor and liquid pressures. It can be seen that the interfacial effect on the vapor pressure and the liquid pressure in the top wick is negligible. However, neglecting the interfacial effect will lead to a smaller liquid pressure drop in the bottom wick.

The boundary and inertial effects on the vapor and liquid pressures are shown in Fig. 6b. The boundary and inertial effects on the vapor pressure are negligible. However, the calculated liquid pressure drop in both top and bottom wicks will be smaller when the boundary and inertial effects are neglected. The larger the injection Reynolds number, the larger the error involved through neglecting the boundary and inertial effects. This is expected, since the liquid flow rate increases with increasing the input heat, hence the error resulted from omitting boundary and inertial effects increases [7]. Figure 7 shows the comparison of the vapor and liquid pressure distributions as well as the vapor temperature distribution calculated with the current model and with the model that employs Darcy's law and assumes the same liquid flow rates at the top and bottom wicks. It can be seen that significant errors occur in calculating vapor and liquid pressures by using the latter model.

Figure 8 shows the interfacial effect and the boundary and inertial effects on the maximum heat transfer capability of the disk-shaped heat pipe. It can be seen that neglecting the vapor–liquid interfacial coupling can lead to an underestimation of the maximum heat transfer capability. This is because the neglection of vapor–liquid interfacial coupling causes the overall liquid pressure drop in the top wick to be larger (Fig. 6a). In contrast, neglecting the boundary and inertial effects causes the overall liquid pressure drop in the top wick to be smaller (Fig. 6b), hence resulting in an overestimation of the maximum heat transfer capability. While the interfacial effect on the maximum heat transfer is smaller, the error involved through neglecting the boundary and inertial effects is significant. Figure 8 also shows the significant error in calculating the maximum heat transfer capability by using the model that employs Darcy's law and assumes the same liquid flow rate at the top and bottom wicks.

To further support the current analysis, the model predictions are compared with the experimental results of North and Avedisian [6] for an ethanol disk-shaped heat pipe. The physical dimensions, wick structure, working fluid and all other parameters of the heat pipe tested by North and Avedisian [6] were used as inputs to our analytical model. The copper disk-shaped heat pipe, 0.149 m diameter, 2.54 cm

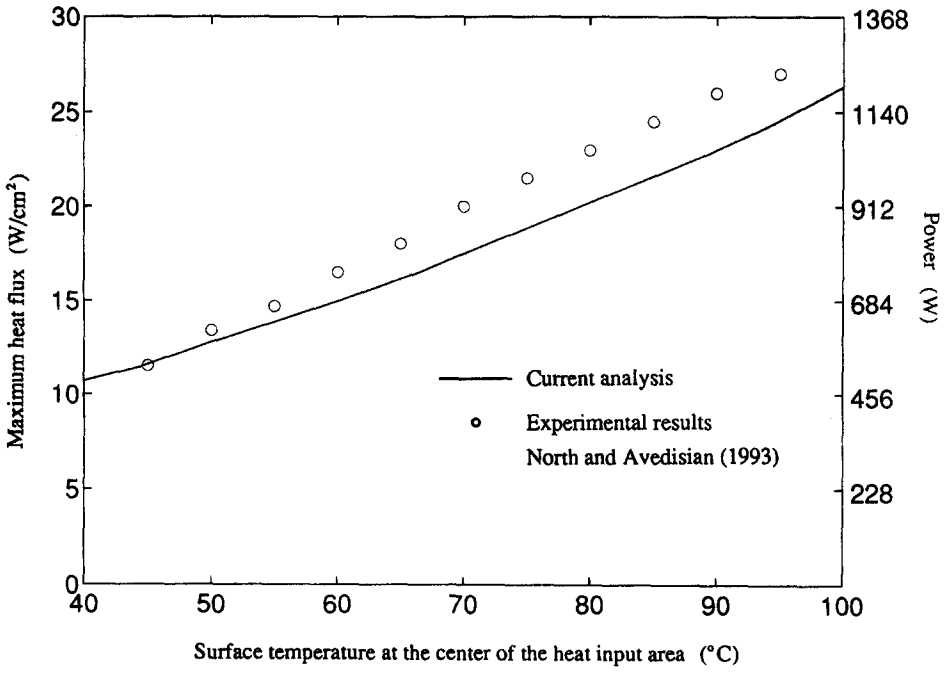

Fig. 9. Comparison of the calculated maximum heat transfer and the experimental data given by North and Avedision [6].

thickness (vapor space + wick) and 0.0762 m diameter of heat input zone, employs sintered copper powder wicks. The thickness of both top and bottom wicks is 0.003 m, and the wick effective pore radius, porosity and permeability are 36 μm, 0.5 and 2.1×10^{-7} cm^2, respectively. The effective thermal conductivity of the liquid–wick region is calculated using the equation given by Dunn and Reay [11] for sintered copper powder with porosity of 0.5. The thermophysical properties of the vapor and liquid are evaluated at the operating temperature. The flow channel angle is taken as 60° in the model. It should be mentioned that the tested heat pipe is heated from below and does not have vertical wicks. The effect of this difference between our model and the tested heat pipe is accounted for through the determination of the permeability of the vertical wicks in our model by matching the predicted maximum heat transfer and the measured data at the beginning of dryout (surface temperature of 45°C [6]). For this test, the permeability of the vertical wicks of 5.0×10^{-9} cm^2 is used. The comparison of the predicted maximum heat transfer with the measured data obtained by North and Avedisian [6] is shown in Fig. 9. It can be seen that the agreement between the experimental results and the model prediction is quite good.

The current analysis is also applied to conventional cylindrical heat pipes. Figure 10 shows the comparison of the analytical results with the numerical results given by Tournier and El-Genk [5] and the experimental results given by Huang *et al.* [12]. It should be mentioned that the calculated vapor temperature in Fig. 10b is the interface temperature. As can be seen in Fig. 10, the analytical results compare very well with both the numerical results given by Tournier and El-Genk [5] and the experimental results given by Huang *et al.* [12]. It should be noted that present results do not represent the optimized maximum heat transfer capability of the disk-shaped heat pipe. Optimization analysis of the heat transfer process within a disk-shaped heat pipe is given in Zhu and Vafai [13].

CONCLUSIONS

A pseudo-three-dimensional analytical model is developed for the vapor and liquid flow in an asymmetrical disk-shaped heat pipe, which incorporates the hydrodynamic coupling of the vapor and liquid flows as well as the gravitational effects, and the effects of non-Darcian transport through the porous wicks. An in-depth analysis of the intra-wick interactions and the phenomenological description of the transport processes within disk-shaped heat pipes are presented. The effect of the vapor–liquid interfacial hydrodynamic coupling and the boundary and inertial effects are analyzed. The results show that the liquid flow in the top and bottom wicks are quite different and significant errors can occur when the same liquid flow rates in the top and bottom wicks is assumed. In addition, neglecting of the hydrodynamic coupling of vapor and liquid flow results in errors in simulating

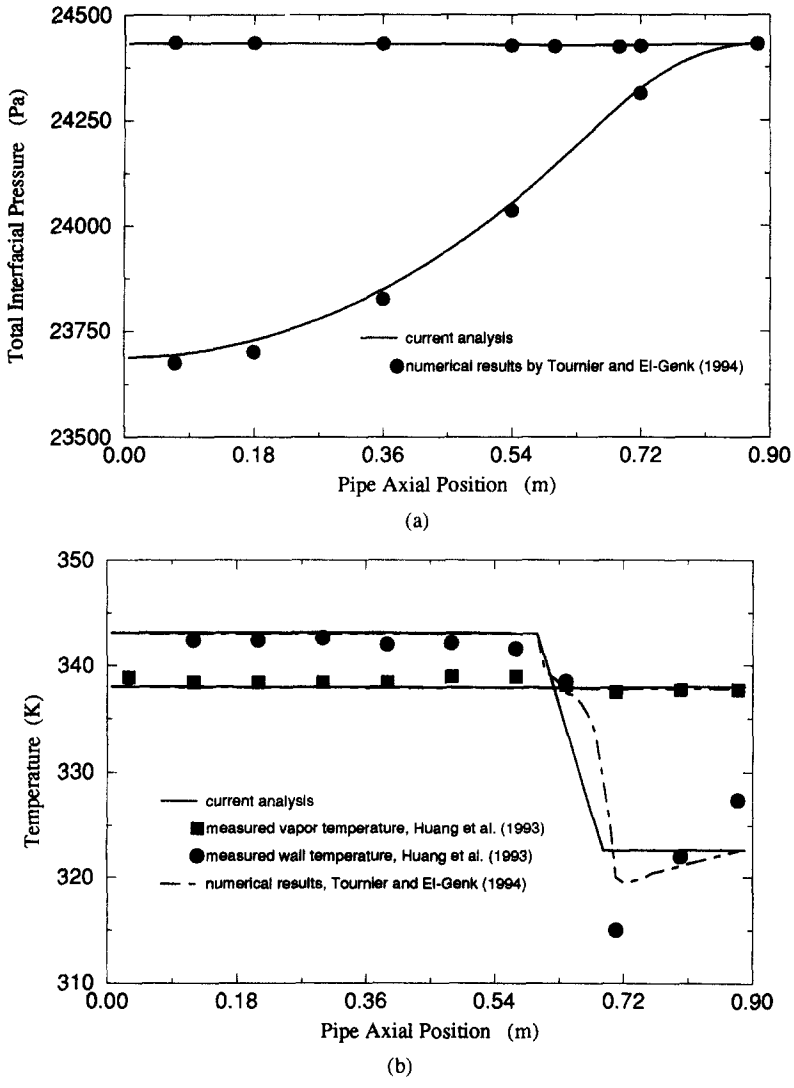

Fig. 10. Comparison of the current model predictions with the numerical results given by Tournier and El-Genk [5] and the experimental results given by Huang *et al.* [12] for a cylindrical heat pipe at steady-state.

both the vapor and the liquid flow fields. While the error caused by the use of Darcy's law which neglects the boundary and inertial effects is negligible in calculating the vapor pressure and temperature, it is significant in calculating the liquid flow rates and pressure drops as well as the maximum heat transfer capability of the heat pipe. Finally, the analytical results are found to compare well with an available experimental study.

Acknowledgements—This work was supported by the Department of Energy under contract number DE-FGO2-89ER60872. The authors would like to thank Dr. Thomas Blue for his help on this work.

REFERENCES

1. K. Vafai and W. Wang, Analysis of flow and heat transfer characteristics of an asymmetrical flat plate heat pipe, *Int. J. Heat Mass Transfer* **35**, 2087–2099 (1992).
2. K. Vafai, N. Zhu and W. Wang, Analysis of asymmetrical disk-shaped and flat plate heat pipes, *ASME J. Heat Transfer* **117**, 209–218 (1995).
3. V. H. Ransom and H. Chow, ATHENA heat pipe transient model, *Trans. 4th Symposium on Space Nuclear Power Systems*, CONF-870102-Summs., Albuquerque, NM, pp. 389–392 (1987).
4. J. M. Doster and M. L. Hall, Numerical modeling of high-temperature liquid-metal heat pipes, 1989 *Joint ASME/A.I.Ch.E. National Heat Tranfers Conference*, Philadelphia, Pennsylvania, Vol. 89-HT-13, pp. 1–9 (1989).
5. J.-M. Tournier and M. S. El-Genk, A heat pipe transient analysis model, *Int. J. Heat Mass Transfer* **37**, 753–762 (1994).
6. M. T. North and C. T. Avedisian, Heat pipe for cooling high flux/high power semiconductor chips, *J. Electron. Packaging* **115**, 112–117 (1993).
7. K. Vafai and C. L. Tien, Boundary and inertia effects on flow and heat transfer in porous media, *Int. J. Heat Mass Transfer* **24**, 195–203 (1981).

8. K. Vafai, Convective flow and heat transfer in variable porosity media, *J. Fluid Mech.* **147,** 233–259 (1984).
9. K. Vafai and R. Thiyagaraja, Analysis of flow and heat transfer at the interface region of a porous medium, *Int. J. Heat Mass Transfer* **30,** 1391–1405 (1987).
10. K. B. Narayana, Vapor flow characteristics of slender cylindrical heat pipes—a numerical approach, *Numer. Heat Transfer* **10,** 79–93 (1986).
11. P. D. Dunn and D. A. Reay, *Heat Pipes*, 3rd edn, Chap. 3. Pergamon Press, New York (1982).
12. L. Huang, M. S. El-Genk and J.-M. Tournier, Transient performance of an inclined water heat pipe with a screen wick, 1993 *ASME National Heat Transfer Conference*, Atlanta, GA, *Heat Pipes and Capillary Pumped Loops* (Edited by A. Faghri, A. J. Juhasz and E. T. Mahefkey), HTD-Vol. 236, pp. 87–92 (1993).
13. N. Zhu and K. Vafai, Optimization analysis of a disk-shaped heat pipe, *AIAA J. Thermophys. Heat Transfer* **10,** 179–182 (1996).